Chapter 2

Transmission Wavefront Shearing Interferometry for Photoelastic Materials

2.1 Introduction

This chapter presents the first analysis of transmission wavefront shearing interferometry for photoelastic materials and experimental verification of the theory. Section 2.2 describes the experimental method and derives the interference pattern first for a general transmission wavefront shearing interferometer, and then specifically for Coherent Gradient Sensing (CGS), from a photoelastic material. Section 2.2.3 describes how phase shifting and polarization optics allow for the determination of the phase related to $\sigma_1 + \sigma_2$. Section 2.3 presents the experimental verification of the analysis for a compressed polycarbonate plate with a side V-notch with good agreement with theoretical data based on a 2D asymptotic solution derived from Williams (1952). The content of this chapter is based on Kramer et al. (2009b), but with more details on the experimental verification.

2.2 Experimental Method and Full-Field Phase Analysis

2.2.1 Experimental Method

The CGS method starts with an incident plane wave of a collimated laser beam that transmits through a transparent specimen or that reflects off an opaque specimen. The working principle of

CGS to laterally shear an incident wavefront, shown in Figure 2.1 for horizontal shear, is the same for both transmission and reflection. Tippur et al. (1991a,b) give a full description of the CGS working principle. The main concept of CGS is that the d_{shear} of the interfered wavefronts is due to diffraction through a pair of Ronchi gratings, G_1 and G_2, each with pitch p, separated by distance $\tilde{\Delta}$ such that the desired wavefronts $\boldsymbol{E_{(0,\pm1)}}$ and $\boldsymbol{E_{(\pm1,0)}}$ are separated by a lateral shearing distance $d_{shear} = \gamma\tilde{\Delta}$ in the x–z or y–z plane and propagate at the same angle γ relative to the z axis upon leaving grating G_2. The diffracted waves transmit through a filtering lens, which separate the corresponding diffraction orders into horizontal diffraction spots at the focal plane of the filtering lens. An aperture at this focal plane selects either the $+1$ or -1 diffraction order, meaning only the wavefronts $\boldsymbol{E_{(0,\pm1)}}$ and $\boldsymbol{E_{(\pm1,0)}}$ propagate to the image plane. In Section 2.2.2, analysis of the first-order diffraction shows how the interference pattern may be related to first x and y derivatives of principal stresses based on assumption of a small d_{shear}.

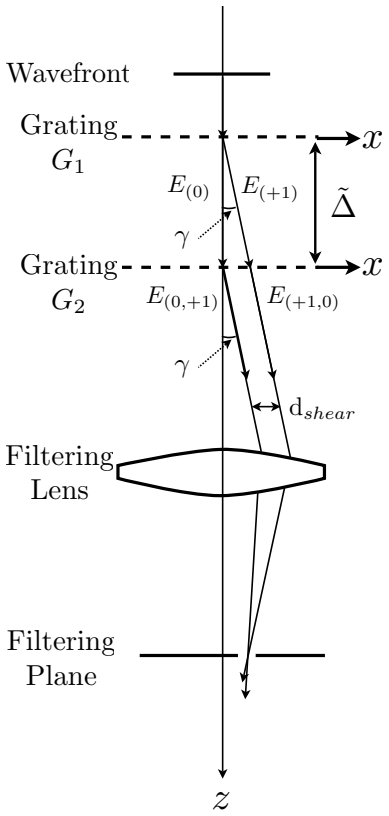

Figure 2.1: Working principle for horizontal shearing transmission CGS

2.2.2 Analysis

2.2.2.1 Electric Field Description of the Transmitted Wavefront

Assuming a coherent plane wave of monochromatic light propagating along the z axis, the electric field of the wavefront at $z = z_o$ is given by

$$\boldsymbol{E}^{in}(x, y, t) = E_x(x, y, t)\hat{\imath} + E_y(x, y, t)\hat{\jmath} \tag{2.1a}$$

$$E_x(x, y, t) = A_x \exp[j(kz_o - \omega t + \phi_x)] \tag{2.1b}$$

$$E_y(x, y, t) = A_y \exp[j(kz_o - \omega t + \phi_y)] \tag{2.1c}$$

where E_x and E_y are the amplitudes, A_x and A_y are constants, λ is the wavelength, $k = 2\pi/\lambda$ is the wave number, ω is the angular frequency, and ϕ_x and ϕ_y are arbitrary constant phase terms. If the plane wave propagates through a transparent material with refractive index n_o and nominal thickness h, then the resulting electric field magnitudes of this perturbed wavefront in the x and y directions after the specimen material at z are

$$E_x^{specimen}(x, y, t) = A_x \exp[j(kz - \omega t + \phi_x + k(n_o - 1)h + k\Delta S_x(x, y))] \tag{2.2a}$$

$$E_y^{specimen}(x, y, t) = A_y \exp[j(kz - \omega t + \phi_y + k(n_o - 1)h + k\Delta S_y(x, y))] \tag{2.2b}$$

where $\Delta S_x(x, y)$ and $\Delta S_y(x, y)$ are the optical path differences at each point (x, y) along the x and y directions, as further described in Section 2.2.2.2.

2.2.2.2 Photoelastic Effect in Transparent Materials

In general, a plane wave transmitted through a material experiences some change in optical path length due to both variation in refractive index, $\Delta n(x, y)$, and variation in thickness, $\Delta h(x, y)$, in the transmitting media. Along a given axis a, the optical path difference is expressed as

$$\Delta S_a(x, y) = h\Delta n_a(x, y) + (n_o - 1)\Delta h(x, y). \tag{2.3}$$

A full explanation of the optical path difference may be found in Papdopoulos (1993). These variations from an initially uniform material can be related to stresses in the material. First, a transparent material that experiences stress-induced birefringence, also known as the photoelastic effect, has variations in refractive index along the three principal optical axes such that

$$\Delta n_1 = n_1 - n_o = A\sigma_1 + B(\sigma_2 + \sigma_3) \tag{2.4a}$$

$$\Delta n_2 = n_2 - n_o = A\sigma_2 + B(\sigma_1 + \sigma_3) \tag{2.4b}$$

$$\Delta n_3 = n_3 - n_o = A\sigma_3 + B(\sigma_1 + \sigma_2) \tag{2.4c}$$

where σ_i, $i = \{1, 2, 3\}$, are the principal stresses and A and B are the two absolute photoelastic constants of the transparent material. These equations are known as the Neumann-Maxwell stress optic law (Coker and Filon, 1993; Frocht, 1941; Narasimhamurty, 1981). In this analysis, the $\hat{p_3}$ principal direction is assumed to be along the z axis. Second, the thickness change in a linear elastic material is related to the principal stresses by Hooke's Law:

$$\Delta h = \Big[\frac{\sigma_3}{E} - \frac{\nu}{E}(\sigma_1 + \sigma_2)\Big]h, \tag{2.5}$$

where E is the Young's modulus, ν is the Poisson's ratio, $\sigma_3 = 0$ for plane stress, and $\Delta h = 0$ for plane strain.

Substituting Equations (2.4a), (2.4b), and (2.5) into Equation (2.3) results in the following two equations for optical path length difference in along the $\hat{p_1}$ and $\hat{p_2}$ principal directions in terms of the sum and difference of principal stresses:

$$\Delta S_1(x, y) = Ch[(\sigma_1 + \sigma_2) + g(\sigma_1 - \sigma_2)] \tag{2.6a}$$

$$\Delta S_2(x, y) = Ch[(\sigma_1 + \sigma_2) - g(\sigma_1 - \sigma_2)] \tag{2.6b}$$

such that

$$C = \frac{A+B}{2} - \frac{\nu}{E}(n_o - 1) \tag{2.7a}$$

$$g = \frac{A-B}{A+B-2\nu(n_o-1)/E} \tag{2.7b}$$

for plane stress, and

$$C = \frac{A+B}{2} + \nu B \tag{2.8a}$$

$$g = \frac{A-B}{A+B+2\nu B} \tag{2.8b}$$

for plane strain. For optically isotropic (nonbirefringent) materials, $A = B$, resulting in $g = 0$; thus, in this case, $\Delta S_1(x,y) = \Delta S_2(x,y) = \Delta S(x,y)$. For optically anistropic (birefringent) materials, $A \neq B$; thus, $\Delta S_1(x,y) \neq \Delta S_2(x,y)$ in general.

2.2.2.3 Electric Field of the Transmitted Wavefront

The incident wavefront given in Equation (2.1) may be written in the orthogonal principal coordinate system at each point (x,y), such that

$$\boldsymbol{E}_p^{in}(x,y,t) = E_1(x,y,t)\hat{p_1} + E_2(x,y,t)\hat{p_2} \tag{2.9a}$$

$$E_1(x,y,t) = E_x(x,y,t)\cos(\alpha) + E_y(x,y,t)\sin(\alpha) \tag{2.9b}$$

$$E_2(x,y,t) = -E_x(x,y,t)\sin(\alpha) + E_y(x,y,t)\cos(\alpha) \tag{2.9c}$$

$$\hat{p_1} = \cos(\alpha)\hat{\imath} + \sin(\alpha)\hat{\jmath} \tag{2.9d}$$

$$\hat{p_2} = -\sin(\alpha)\hat{\imath} + \cos(\alpha)\hat{\jmath}, \tag{2.9e}$$

where α is the angle between the Cartesian and principal coordinate systems. The effect of transmission through a birefringent plate is the gain of a phase of $k\Delta S_{1,2}$ along the principal directions,

resulting in a transmitted wavefront in the principal coordinate system of

$$\boldsymbol{E}_p^{specimen}(x,y,t) = E_1(x,y,t)\exp[jk\Delta S_1(x,y)]\hat{p_1} + E_2(x,y,t)\exp[jk\Delta S_2(x,y)]\hat{p_2}. \tag{2.10}$$

2.2.2.4 Analysis of Interference Pattern

As described in Section 2.2.1, the interference of wavefronts $\boldsymbol{E_{(0,\pm 1)}}$ and $\boldsymbol{E_{(\pm 1,0)}}$ is the interference of two identical wavefronts $\boldsymbol{E}^{\pm 1}$ that are separated by distance d_{shear}, as written in Equation (2.11) for the lateral shearing of the electric field in the x direction with the electric field in the principal coordinate system:

$$\boldsymbol{E}_p^{image}(x,y) = E_1^{image}(x,y)\hat{p_1} + E_2^{image}(x,y)\hat{p_2} \tag{2.11a}$$

$$E_1^{image}(x,y) = E_1^{\pm 1}(x,y) + E_1^{\pm 1}(x + d_{shear}, y) \tag{2.11b}$$

$$E_2^{image}(x,y) = E_2^{\pm 1}(x,y) + E_2^{\pm 1}(x + d_{shear}, y) \tag{2.11c}$$

$$\begin{aligned} E_1^{\pm 1}(x,y) = {} & A_x^{\pm 1}\cos(\alpha)\exp[j(kz - \omega t + \phi_x + k\Delta S_1(x,y))] \\ & + A_y^{\pm 1}\sin(\alpha)\exp[j(kz - \omega t + \phi_y + k\Delta S_1(x,y))] \end{aligned} \tag{2.11d}$$

$$\begin{aligned} E_2^{\pm 1}(x,y) = {} & -A_x^{\pm 1}\sin(\alpha)\exp[j(kz - \omega t + \phi_x + k\Delta S_2(x,y))] \\ & + A_y^{\pm 1}\cos(\alpha)\exp[j(kz - \omega t + \phi_y + k\Delta S_2(x,y))], \end{aligned} \tag{2.11e}$$

where constants $A_x^{\pm 1} < A_x$ and $A_y^{\pm 1} < A_y$ due to diffraction. The resulting irradiance (intensity) of the interfered wavefronts, I^{image}, in Equation (2.12), is the superposition of the irradiance of the E_1 component, I_1^{image}, and the irradiance of the E_2 component, I_2^{image}, since the principal directions are orthogonal:

$$I^{image} = \langle E_1^{image} E_1^{image*}\rangle_t + \langle E_2^{image} E_2^{image*}\rangle_t = I_1^{image} + I_2^{image} \tag{2.12a}$$

$$
\begin{aligned}
I_1^{image} &= 2(A_x^{\pm 1})^2\cos^2(\alpha) + 2(A_y^{\pm 1})^2\sin^2(\alpha) + 4A_x^{\pm 1}A_y^{\pm 1}\cos(\alpha)\sin(\alpha)\cos(\phi_x - \phi_y) \\
&\quad + \{2(A_x^{\pm 1})^2\cos^2(\alpha) + 2(A_y^{\pm 1})^2\sin^2(\alpha)\}\cos[k\Delta S_1(x,y) - k\Delta S_1(x + d_{shear}, y)] \\
&\quad + 2A_x^{\pm 1}A_y^{\pm 1}\cos(\alpha)\sin(\alpha)\{\cos[\phi_x - \phi_y + k\Delta S_1(x,y) - k\Delta S_1(x + d_{shear}, y)] \\
&\qquad + \cos[\phi_y - \phi_x + k\Delta S_1(x,y) - k\Delta S_1(x + d_{shear}, y)]\} \qquad (2.12b) \\
I_2^{image} &= 2(A_x^{\pm 1})^2\sin^2(\alpha) + 2(A_y^{\pm 1})^2\cos^2(\alpha) - 4A_x^{\pm 1}A_y^{\pm 1}\cos(\alpha)\sin(\alpha)\cos(\phi_x - \phi_y) \\
&\quad + \{2(A_x^{\pm 1})^2\sin^2(\alpha) + 2(A_y^{\pm 1})^2\cos^2(\alpha)\}\cos[k\Delta S_2(x,y) - k\Delta S_2(x + d_{shear}, y)] \\
&\quad - 2A_x^{\pm 1}A_y^{\pm 1}\cos(\alpha)\sin(\alpha)\{\cos[\phi_x - \phi_y + k\Delta S_2(x,y) - k\Delta S_2(x + d_{shear}, y)] \\
&\qquad + \cos[\phi_y - \phi_x + k\Delta S_2(x,y) - k\Delta S_2(x + d_{shear}, y)]\}. \qquad (2.12c)
\end{aligned}
$$

Therefore, the resultant image is the following:

$$
\begin{aligned}
I^{image} &= 2(A_x^{\pm 1})^2 + 2(A_y^{\pm 1})^2 \\
&\quad + \{2(A_x^{\pm 1})^2\cos^2(\alpha) + 2(A_y^{\pm 1})^2\sin^2(\alpha) + 4A_x^{\pm 1}A_y^{\pm 1}\cos(\alpha)\sin(\alpha)\cos(\phi_x - \phi_y)\} \\
&\qquad \cos[k(\Delta S_1(x,y) - \Delta S_1(x + d_{shear}, y))] \\
&\quad + \{2(A_x^{\pm 1})^2\sin^2(\alpha) + 2(A_y^{\pm 1})^2\cos^2(\alpha) - 4A_x^{\pm 1}A_y^{\pm 1}\cos(\alpha)\sin(\alpha)\cos(\phi_x - \phi_y)\} \\
&\qquad \cos[k(\Delta S_2(x,y) - \Delta S_2(x + d_{shear}, y))]. \qquad (2.13)
\end{aligned}
$$

The shearing distance is usually small compared to the field of view of the image ($L^f \times W^f$), so the phase terms of I_1^{image} and I_2^{image}, denoted $\varphi_{1,2}(x,y)$, can be related to the derivatives of $\Delta S_{1,2}$. For $(d_{shear}/\{L^f, W^f\}) \ll 1$,

$$
\varphi_{1,2} = k(\Delta S_{1,2}(x,y) - \Delta S_{1,2}(x + \Delta x, y)) \approx k d_{shear}\frac{\partial \Delta S_{1,2}(x,y)}{\partial x}. \qquad (2.14)
$$

Substituting $\Delta S_{1,2}$ from Equations (2.6a) and (2.6b) into Equation (2.14) connects the phase terms

of the interference patterns to stresses:

$$\varphi_{1,2} = kd_{shear}Ch\Big[\frac{\partial(\sigma_1+\sigma_2)}{\partial x} \pm g\frac{\partial(\sigma_1-\sigma_2)}{\partial x}\Big]. \tag{2.15}$$

The equation for the image may be written in terms of two phases, one related to $\sigma_1+\sigma_2$ and the other related to $\sigma_1-\sigma_2$ as follows:

$$I^{image} = I_o + I_{1o}\cos[\varphi_{sum}+\varphi_{diff}] + I_{2o}\cos[\varphi_{sum}-\varphi_{diff}] \tag{2.16a}$$

$$I_o = 2(A_x^{\pm1})^2 + 2(A_y^{\pm1})^2 \tag{2.16b}$$

$$I_{1o} = 2(A_x^{\pm1})^2\cos^2(\alpha) + 2(A_y^{\pm1})^2\sin^2(\alpha) + 4A_x^{\pm1}A_y^{\pm1}\cos(\alpha)\sin(\alpha)\cos(\phi_x-\phi_y) \tag{2.16c}$$

$$I_{2o} = 2(A_x^{\pm1})^2\sin^2(\alpha) + 2(A_y^{\pm1})^2\cos^2(\alpha) - 4A_x^{\pm1}A_y^{\pm1}\cos(\alpha)\sin(\alpha)\cos(\phi_x-\phi_y) \tag{2.16d}$$

$$\varphi_{sum} = kd_{shear}Ch\frac{\partial(\sigma_1+\sigma_2)}{\partial x} \tag{2.16e}$$

$$\varphi_{diff} = kd_{shear}Chg\frac{\partial(\sigma_1-\sigma_2)}{\partial x}. \tag{2.16f}$$

Since the intensity contains a sum of two sinusoids with the same frequency k, then Equation (2.16a) may be written as a single interference pattern with a phase that is the sum of φ_{sum} and a compound phase φ_c:

$$I^{image} = I_o + I_c\cos[\varphi_{sum}+\varphi_c] \tag{2.17a}$$

$$I_c = \sqrt{I_{1o}^2 + I_{2o}^2 + 2I_{1o}I_{2o}\cos(2\varphi_{diff})} \tag{2.17b}$$

$$\varphi_c = \arctan\Big[\frac{(I_{1o}-I_{2o})\sin(\varphi_{diff})}{(I_{1o}+I_{2o})\cos(\varphi_{diff})}\Big]. \tag{2.17c}$$

A similar result for the y direction shearing may be obtained from the previous analysis, except the derivatives are with respect to y instead of x.

For the specific case of CGS, d_{shear} is $\tilde{\Delta}\lambda/p$, with $k = 2\pi/\lambda$, such that Equations (2.16e) and

(2.16f) become the following:

$$\varphi_{sum} = \frac{2\pi\tilde{\Delta}Ch}{p}\frac{\partial(\sigma_1+\sigma_2)}{\partial x} \tag{2.18a}$$

$$\varphi_{diff} = \frac{2\pi\tilde{\Delta}Chg}{p}\frac{\partial(\sigma_1-\sigma_2)}{\partial x}. \tag{2.18b}$$

For linearly elastic, optically isotropic materials with $g = 0$, then $\varphi_{diff} = 0$, which leads to the classic result for the image irradiance, $I^{isotropic} = I_o\{1+\cos[\varphi_{sum}]\}$, where the phase term of the interference pattern is related only to the derivative of the sum of principal stresses (Tippur et al., 1991b). As shown above, unlike optically isotropic materials, photoelastic materials produce complicated interference patterns that are difficult to interpret. Fortunately, phase shifting methods in conjunction with incident polarized light allow for the recovery of φ_{sum}, and thus the x or y derivative of $\sigma_1+\sigma_2$, in full field.

2.2.3 Phase Separation and Interpretation

2.2.3.1 Four-Step Phase Shifting

The phase-shifting interferometry technique used for CGS in this study is a four-step technique with $\pi/2$ phase steps, induced by a lateral shift of $p/4$ in one Ronchi grating in the direction of the dominant lateral shearing, resulting in four phase-shifted interference patterns. For an optically isotropic material, the resultant intensities, which are functions of a single phase term φ, are $I_1 = I_o(1+\cos(\varphi))$, $I_2 = I_o(1+\cos(\varphi+\pi/2))$, $I_3 = I_o(1+\cos(\varphi+\pi))$, and $I_4 = I_o(1+\cos(\varphi+3\pi/2))$. The original phase map, φ, is related to these intensities by

$$\varphi = \arctan\left[\frac{I_4-I_2}{I_1-I_3}\right] = \arctan\left[\frac{\sin(\varphi)}{\cos(\varphi)}\right]. \tag{2.19}$$

This equation yields a "wrapped" phase map with discontinuities of height $h_d = 2\pi$ since the range of an arctan() formula is 2π when the signs of the numerator and denominator are known. The full range of φ is determined by unwrapping the phase term from the arctan() formula, as described in

Section 2.3.

For optically anisotropic materials for a general initial electric field, from Equation (2.17), the four phase-shifted images are

$$I_1 = I_o + I_c \cos[\varphi_{sum} + \varphi_c] \tag{2.20a}$$

$$I_2 = I_o + I_c \cos[\varphi_{sum} + \varphi_c + \tfrac{\pi}{2}] \tag{2.20b}$$

$$I_3 = I_o + I_c \cos[\varphi_{sum} + \varphi_c + \pi] \tag{2.20c}$$

$$I_4 = I_o + I_c \cos[\varphi_{sum} + \varphi_c + \tfrac{3\pi}{2}]. \tag{2.20d}$$

The phase map of $\varphi_{sum} + \varphi_c$ may be recovered using the typical arctan() formula similar to Equation (2.19) such that

$$\varphi_{sum} + \varphi_c = \arctan\left[\frac{I_4 - I_2}{I_1 - I_3}\right] = \arctan\left[\frac{I_c \sin(\varphi_{sum} + \varphi_c)}{I_c \cos(\varphi_{sum} + \varphi_c)}\right], \tag{2.21}$$

but Equation (2.21) is indeterminate when $I_c = 0$, so this equation is only true for $I_c \neq 0$. Specifically polarized input electric fields allow for separation of φ_{sum} from φ_c, as discussed below.

2.2.3.2 Two Methods for Determination of the First Derivative of $\sigma_1 + \sigma_2$

The first method to recover φ_{sum} involves capturing images from a pure $E_x\hat{\imath}$ input electric field and from a pure $E_y\hat{\jmath}$ input electric field. From Equation (2.17), for $A_x = A_o$ and $A_y = 0$, and thus $A_x^{\pm 1} = A_o^{\pm 1}$ and $A_y^{\pm 1} = 0$, the image is

$$I^{Ex} = I_o^{Ex} + I_c^{Ex} \cos[\varphi^{Ex}] \tag{2.22a}$$

$$\varphi^{Ex} = \varphi_{sum} + \varphi_{\alpha d} \tag{2.22b}$$

$$I_o^{Ex} = 2(A_o^{\pm 1})^2 \tag{2.22c}$$

$$I_c^{Ex} = I_o^{Ex} \sqrt{1 - \sin^2(2\alpha) \sin^2(\phi_{diff})} \tag{2.22d}$$

$$\varphi_{\alpha d} = \arctan[\cos(2\alpha) \tan(\phi_{diff})] \tag{2.22e}$$

where $\varphi_{\alpha d}$ is a compound phase related to α and φ_{diff}. Similarly, for $A_x = 0$ and $A_y = A_o$, and thus $A_x^{\pm 1} = 0$ and $A_y^{\pm 1} = A_o^{\pm 1}$ from Equation (2.17), the image is

$$I^{Ey} = I_o^{Ey} + I_c^{Ey} \cos[\varphi^{Ey}] \tag{2.23a}$$

$$\varphi^{Ey} = \varphi_{sum} - \varphi_{\alpha d} \tag{2.23b}$$

$$I_o^{Ey} = 2(A_o^{\pm 1})^2 \tag{2.23c}$$

$$I_c^{Ey} = I_o^{Ey} \sqrt{1 - \sin^2(2\alpha) \sin^2(\phi_{diff})}. \tag{2.23d}$$

If phase-shifted images for these two configurations are taken for the same field of view for the same deformation state in the specimen, then the φ^{Ex} and φ^{Ey} fields are calculated by Equation (2.21). For both of these fields, Equation (2.21) does not hold for $\sqrt{1 - \sin^2(2\alpha) \sin^2(\phi_{diff})} = 0$, but this is likely true for only a few points in the field of view. Since I_c^{Ex} and I_c^{Ey} are always nonnegative, then Equation (2.21) can express the absolute signs of the numerator and denomiator separately for each configuration, and the height discontinuity of the wrapped phases are $h_d = 2\pi$, as explained in Section 2.2.3.1. After unwrapping these fields, φ_{sum} may be separated from the other phase, meaning $\varphi_{sum} = (\varphi^{Ex} + \varphi^{Ey})/2$. Additionally, $\varphi_{\alpha d} = (\varphi^{Ex} - \varphi^{Ey})/2 = \arctan[\cos(2\alpha) \tan(\phi_{diff})]$. Section 2.2.3.3 describes possible configurations of polarization optics to achieve this case.

Another possible method for determining φ_{sum} only requires one set of phase-shifted images. If the input electric field is circularly polarized such that $A_x = A_y = A_o/\sqrt{2}$, $\phi_x = \phi_y \pm \pi/2$, and consequently $A_x^{\pm 1} = A_y^{\pm 1} = A_o^{\pm 1}/\sqrt{2}$ using polarization optics, then the image given in Equation (2.17) may be simplified to

$$I^{circ} = I_o^{circ} + I_c^{circ} \cos[\varphi_{sum}] \tag{2.24a}$$

$$I_o^{circ} = 2(A_o^{\pm 1})^2 \tag{2.24b}$$

$$I_c^{circ} = I_o^{circ} \cos[\varphi_{diff}]. \tag{2.24c}$$

If phase-shifted images for this configuration are analyzed using Equation (2.21), then φ_{sum} is

determined by

$$\varphi_{sum} = \arctan\left[\frac{I_4 - I_2}{I_1 - I_3}\right] = \arctan\left[\frac{\sin(\varphi_{sum})\cos(\varphi_{diff})}{\cos(\varphi_{sum})\cos(\varphi_{diff})}\right]. \tag{2.25}$$

This equation is only true for (x, y) coordinates where $\cos(\varphi_{diff}) \neq 0$, since the argument of the arctan() is indeterminate where $\cos(\varphi_{diff}) = 0$. Since $\cos(\varphi_{diff})$ is in the numerator and the denominator, the argument to the arctan() formula in Equation (2.25) cannot express the absolute signs of the numerator and denominator separately, so an arctan() algorithm that gives values from $-\pi/2$ to $\pi/2$ should be used. Thus, the wrapped phase term from this formula should have discontinuities of height $h_d = \pi$ instead of 2π. If the other arctan() algorithm that gives values from $-\pi$ to π is used, then the wrapped phase term is incorrect. After unwrapping, with the full range of φ_{sum} from wavefront shearing in the x direction and Equation (2.18a), the full-field x-derivative of $\sigma_1 + \sigma_2$ may be determined by

$$\frac{\partial(\sigma_1 + \sigma_2)}{\partial x} = \frac{p}{2\pi\tilde{\Delta}Ch}\varphi_{sum}. \tag{2.26}$$

2.2.3.3 Polarization Optics

Polarization optics, such as a linear polarizer, $\lambda/2$ plate, and $\lambda/4$ plate, allow for manipulation of the input electric field. A general schematic of configurations useful here is shown in Figure 2.2. To obtain pure $E_x\hat{\imath}$ or $E_y\hat{\jmath}$ fields with only a simple change required to switch between the two inputs, a polarizer and a $\lambda/2$ plate are used; this combination of optics also gives the same range of intensity for both input types, allowing for optimization of the intensity for the experimental equipment, helping to prevent camera saturation. The objective is to start with either pure $E_x\hat{\imath}$ or $E_y\hat{\jmath}$ after the polarizer at $\rho = m\pi/2$, m integer, then maintain that field through the $\lambda/2$ plate with $\xi = \rho$ for the first image, and then obtain the opposite field by setting the $\lambda/2$ to $\xi = \rho \pm (2n+1)\pi/4$, n integer.

To create circularly polarized light, the collimated laser beam passes through a polarizer with polarization axis at angle ρ to the x axis and then through a $\lambda/4$ plate with fast axis at angle ξ to the x axis with $\rho - \xi = \pm\pi/4$. Other combinations of optics can produce the desired equal amplitudes

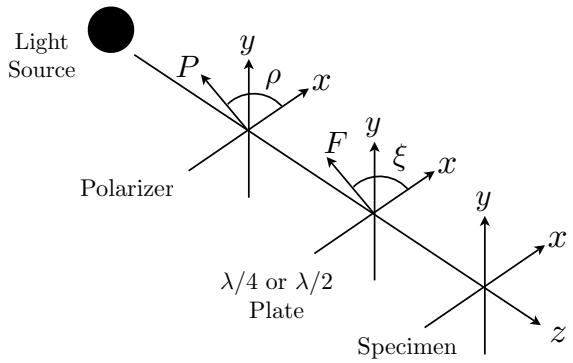

Figure 2.2: Polarization optics before the transparent specimen: two configurations with either a $\lambda/4$ or $\lambda/2$ plate before the specimen

of the E_x and E_y fields, but for clarity and simplicity, these two configurations are considered here. Table 2.1 gives the specific polarization optic configurations used in this study, stating the angles of the optics, the amplitudes of the electric field components, and the resultant phase term of the interference pattern in Equation (2.17).

ρ of Polarizer	ξ of $\lambda/4$ Plate	ξ of $\lambda/2$ Plate	$\lvert E_x \rvert$	$\lvert E_y \rvert$	Phase Determined
0	$\pi/4$	-	$A_x/\sqrt{2}$	$A_x/\sqrt{2}$	φ_{sum}
0	-	0	A_x	0	$\varphi_{sum} + \varphi_{\alpha d}$
0	-	$\pi/4$	0	A_x	$\varphi_{sum} - \varphi_{\alpha d}$

Table 2.1: Polarization optic configurations used in this study

2.3 Experimental Verification

The experimental verification was performed on a 12.7 mm × 12.7 mm square plate with thickness $h = 1.0$ mm and with a 60^o V-notch cut out of the side of the plate, as shown in Figure 2.3. The depth of the V-notch, d, is 6.35 mm, and the V-notch opening width, w, is 7.34 mm. The plate is polycarbonate, which is a thermoplastic polymer that is highly photoelastic, with absolute photoelastic constants $A = -2.45 \times 10^{-11}$ m^2/N and $B = -9.38 \times 10^{-11}$ m^2/N (Shimizu et al., 1998). This plastic has a Young's modulus of $E = 2.3$ GPa, Poisson's ratio of $\nu = 0.36$, and refractive index

of $n_o = 1.586$. The photoelasticity-related constants used in calculating φ_{sum} and φ_{diff} are therefore $C = 1.51 \times 10^{-10}$ m^2/N and $g = 0.23$. The specimen is from a polycarbonate sheet with residual stress due to forming; for this specimen in the field of view, the through-thickness average residual stresses are determined to be $\sigma_{xx}^{resid} \approx 1.59$ MPa, $\sigma_{yy}^{resid} \approx -1.9$ MPa, and $\sigma_{xy}^{resid} \approx -0.1$ MPa. This residual stress is assumed to be constant throughout the field of view. The procedure for determining these residual stresses is explained in Section 3.3.

In the following example, the specimen is compressed by 14.5 N (1.14 MPa) along the y axis. The experimental optical parameters are the following: the monochromatic CCD camera is the IMPERX IPX-1M48-L with a 1000×1000 pixel chip; the field of view is 3.77 mm $\times$ 3.77 mm; the image resolution is 3.8 μm; the Ronchi grating pitch, p, is 1 mm/40; the grating separation, $\tilde{\Delta}$, is 12.48 mm; the wavelength of light from the linearly polarized HeNe laser is 632. nm; and the lateral shearing distance, d_{shear}, is 313 μm.

Williams (1952) presented a derivation of the stress fields of a thin plate with an "angular corner" cut out of it under uniaxial tensile load with various boundary conditions. This derivation most commonly utilized for the derivation of the stress field of a Mode I crack, which is a corner of angle 0^o, in a plate. Here, the derivation is applied to a thin plate with a 60^o V-shaped notch under uniaxial compression, as shown in Figure 2.3, and is detailed in Appendix B. The 2D stress solution in polar coordinates is as follows:

$$\sigma_{rr}(r,\theta) = \frac{C_f \sigma_{app} d^{1-\lambda_o}}{(r)^{1-\lambda_o}} \Big\{ -\lambda_o(\lambda_o+1)\cos[(\lambda_o+1)\theta] + \lambda_o(\lambda_o-3)\frac{\cos[(\lambda_o+1)\frac{\zeta}{2}]}{\cos[(\lambda_o-1)\frac{\zeta}{2}]}\cos[(\lambda_o-1)\theta] \Big\}, \tag{2.27a}$$

$$\sigma_{\theta\theta}(r,\theta) = \frac{C_f \sigma_{app} d^{1-\lambda_o} \lambda_o(\lambda_o+1)}{(r)^{1-\lambda_o}} \Big\{ \cos[(\lambda_o+1)\theta] - \frac{\cos[(\lambda_o+1)\frac{\zeta}{2}]}{\cos[(\lambda_o-1)\frac{\zeta}{2}]}\cos[(\lambda_o-1)\theta] \Big\}, \tag{2.27b}$$

$$\sigma_{r\theta}(r,\theta) = \frac{C_f \sigma_{app} d^{1-\lambda_o} \lambda_o}{(r)^{1-\lambda_o}} \Big\{ (\lambda_o+1)\sin[(\lambda_o+1)\theta] - (\lambda_o-1)\frac{\cos[(\lambda_o+1)\frac{\zeta}{2}]}{\cos[(\lambda_o-1)\frac{\zeta}{2}]}\sin[(\lambda_o-1)\theta] \Big\}, \tag{2.27c}$$

where σ_{app} is the far-field applied stress, $\lambda_o = 0.512221$ for a 60^o V-notch, C_f is a fitting parameter depending on specimen geometry, $\zeta = 5\pi/3$ is material remaining after V-notch is cut out, and d is the depth of the V-notch. A constant residual stress, as given above for this specimen, is added to this theoretical stress field solution in Equations (2.27a)–(2.27c). For this particular example, the applied stress σ_{app} is -1.39MPa, and the fitting parameter C_f is 0.57, as determined by comparing the experimental and theoretical in-plane stress fields. The equations for the x derivatives of $\sigma_1 + \sigma_2$ and of $\sigma_1 - \sigma_2$ in terms of the polar stresses, α and θ is provided in Appendix A.

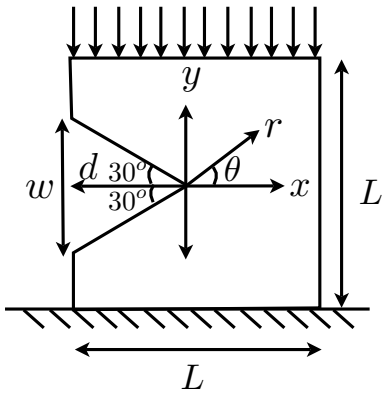

Figure 2.3: Schematic of a compressed polycarbonate plate with a side V-notch

2.3.1 Images for Compressed Polycarbonate Specimen

Figure 2.4 shows the experimental and theoretical images of I_1 for horizontal shear of the configuration shown in Figure 2.3. In Figures 2.4(a) and 2.4(c), the images for the pure $E_x\hat{\imath}$ and pure $E_y\hat{\jmath}$ fields, respectively, have interference fringes with good fringe contrast because I_c^{Ex} and I_c^{Ey} vary little in the field of view. The image in Figure 2.4(e) of the $|E_x| = |E_y|$ fields using the $\lambda/4$ plate method shows discontinuous fringes, evidence of $I_c^{circ} = I_o^{circ}\cos(\varphi_{diff})$ modulating $\cos(\varphi_{sum})$. Clearly, these interference patterns cannot yield the desired phase terms as they are, but require phase shifting. Figures 2.4(b), 2.4(d), and 2.4(f) are the theoretical images for the pure $E_x\hat{\imath}$, pure $E_y\hat{\jmath}$, and $|E_x| = |E_y|$ input fields, which compare well to the experimental fields in shape and fringe density. The residual stress may not be uniform near the V-notch cut-out because some of the residual stress may be relieved during specimen preparation; since the theoretical field is based on a

uniform residual stress assumption, then the theoretical and experimental α have slight differences for $|\theta| > \pi/2$, resulting in slight shape differences in comparing theoretical and experimental images for $|\theta| > \pi/2$. The slightly larger lobes near $\theta = 0$ are mostly likely due to slightly higher applied stress on this side because of nonuniform compressive loading. Despite these slight differences due to experimental error and residual stress in the material, near $\theta = 0$, the experimental image from the pure $E_x\hat{\imath}$ input has the expected wider lobe, the experimental image from the $E_y\hat{\jmath}$ input has the expected narrower lobe, and the experimental image from the $|E_x| = |E_y|$ input field indicates the same interference beading as the theoretical image. Figures 2.5, 2.6, and 2.7 show the sets of four experimental phase-shifted images for pure $E_x\hat{\imath}$ input, pure $E_y\hat{\imath}$ input, and circularly polarized electric field input, respectively. The interference patterns within a set of phase-shifted images clearly are slightly different, though they have the same fringe density and shape, indicating a constant phase shift added to the interference pattern over the entire field between each subsequent phase-shifted image. The part of the image with the V-notch cut-out clearly shows a uniform $\pi/2$ phase shift in the intensity between the images since this part of the image comes from light passing through air, which does not change with load like the intensity from the specimen does.

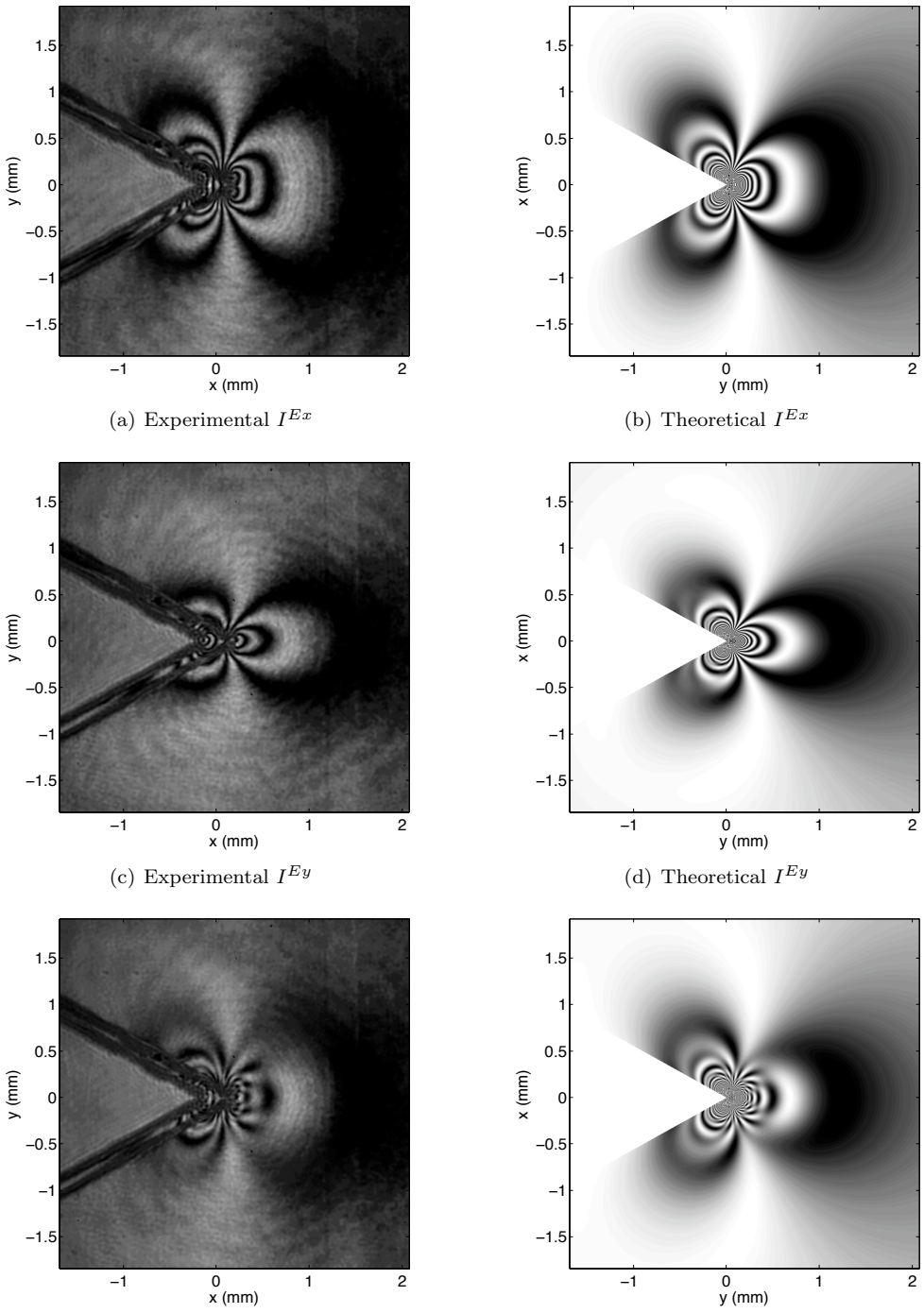

(a) Experimental I^{Ex}

(b) Theoretical I^{Ex}

(c) Experimental I^{Ey}

(d) Theoretical I^{Ey}

(e) Experimental I^{circ}

(f) Theoretical I^{circ}

Figure 2.4: Experimental and theoretical images for horizontal shear with good comparison: (a) experimental $I^{Ex} = I_o^{Ex} + I_c^{Ex}\cos[\varphi_{sum} + \varphi_{\alpha d}]$; (b) theoretical $I^{Ex} = I_o^{Ex} + I_c^{Ex}\cos[\varphi_{sum} + \varphi_{\alpha d}]$; (c) experimental $I^{Ey} = I_o^{Ey} + I_c^{Ey}\cos[\varphi_{sum} - \varphi_{\alpha d}]$; (d) theoretical $I^{Ey} = I_o^{Ey} + I_c^{Ey}\cos[\varphi_{sum} - \varphi_{\alpha d}]$; (e) experimental $I^{circ} = I_o^{circ} + I_o^{circ}\cos[\varphi_{diff}]\cos[\varphi_{sum}]$; and (f) theoretical $I^{circ} = I_o^{circ} + I_o^{circ}\cos[\varphi_{diff}]\cos[\varphi_{sum}]$ [Note: V-notch region masked in white in theoretical images]

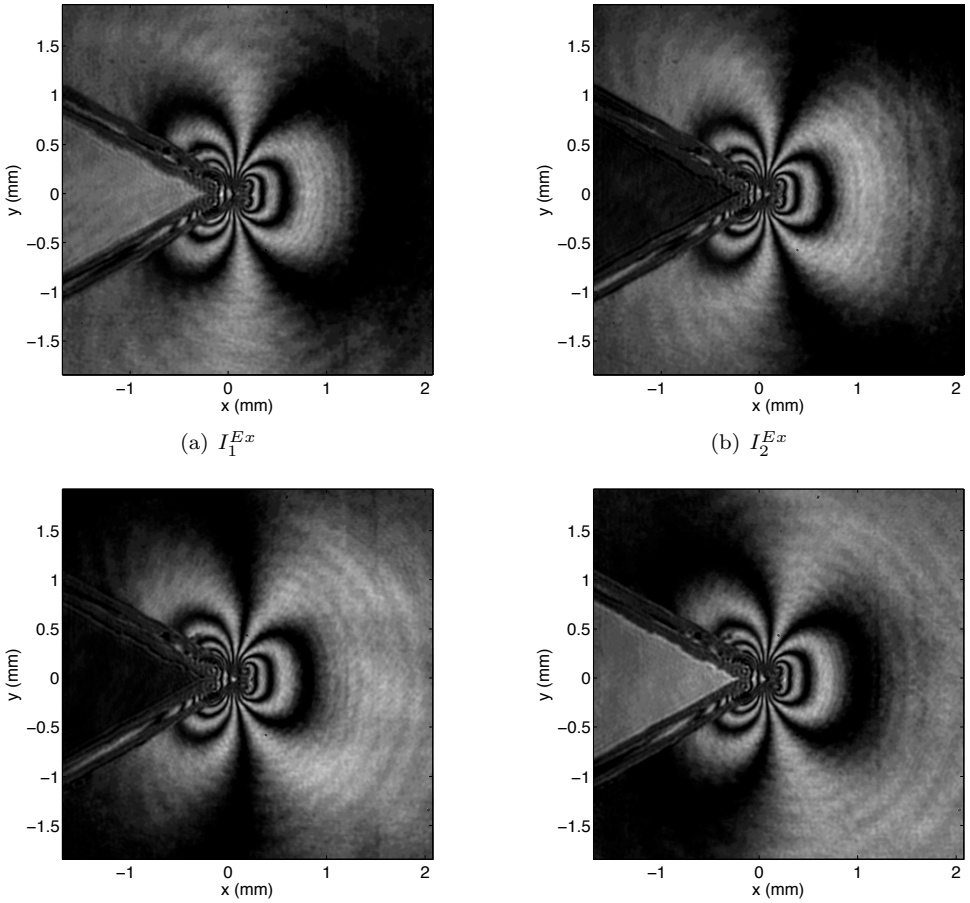

(a) I_1^{Ex} (b) I_2^{Ex}

(c) I_3^{Ex} (d) I_4^{Ex}

Figure 2.5: Experimental phase-shifted images from horizontal shearing CGS using pure $E_x\hat{\imath}$ input for compressed polycarbonate V-notch plate

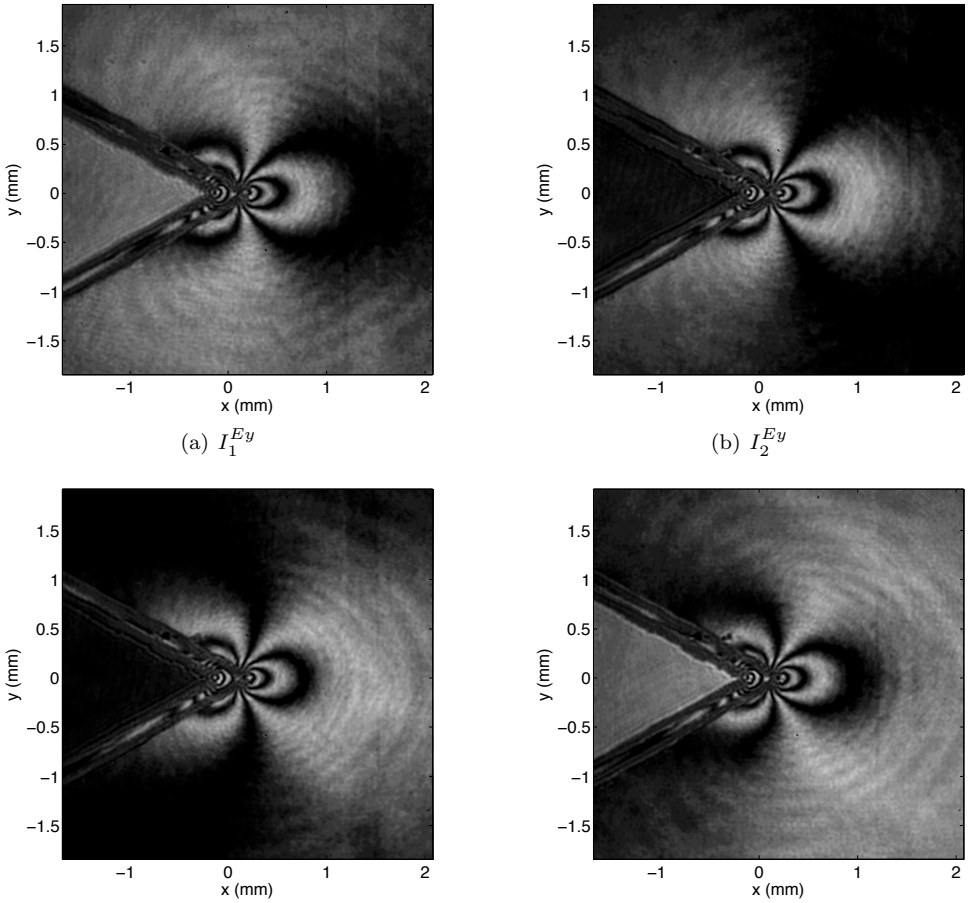

(a) I_1^{Ey} (b) I_2^{Ey}

(c) I_3^{Ey} (d) I_4^{Ey}

Figure 2.6: Experimental phase-shifted images from horizontal shearing CGS using pure $E_y\hat{j}$ input for compressed polycarbonate V-notch plate

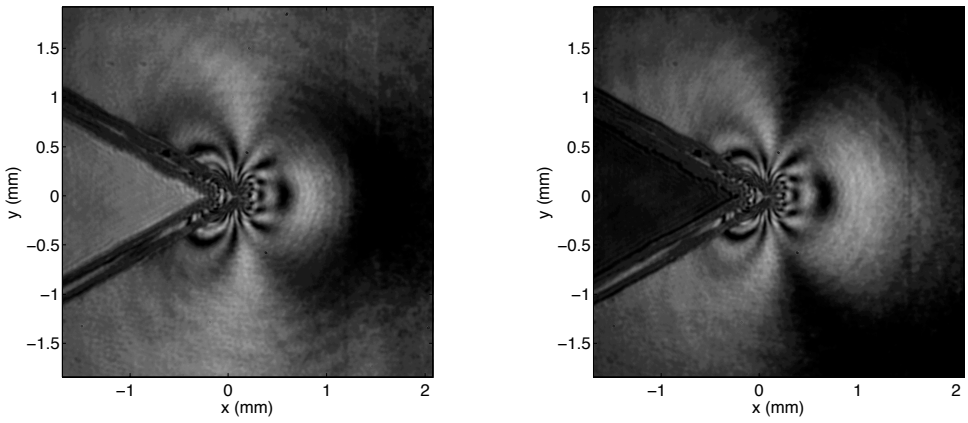

(a) I_1^{circ}

(b) I_2^{circ}

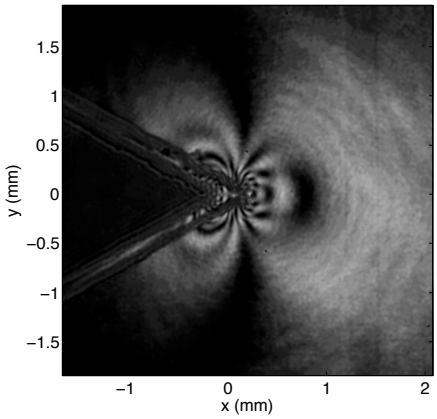

(c) I_3^{circ}

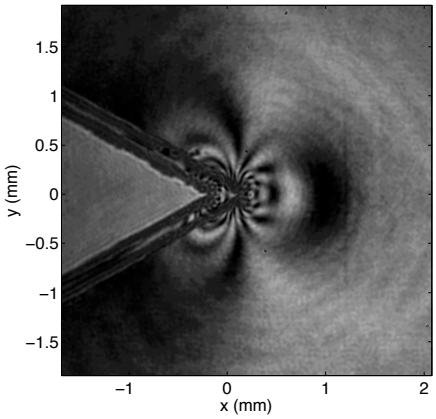

(d) I_4^{circ}

Figure 2.7: Experimental phase-shifted images from horizontal shearing CGS using the $\lambda/4$ polarization method for compressed polycarbonate V-notch plate

2.3.2 Image Analysis

Figure 2.8 includes the experimental and theoretical wrapped phase fields for φ^{Ex} and φ^{Ey}. The general three-lobed shape in each experimental field compares well with the theoretical fields, though the differences between the theoretical and experimental are most likely due to slightly nonuniform compressive loading of the specimen. The experimental and theoretical wrapped phase field for the φ_{sum} from Equation (2.25) from the $\lambda/4$ plate method and the theoretical $\cos(\varphi_{diff})$ field are shown in Figure 2.9. In Figure 2.9(a), the fringes have regions in a four-lobed clover leaf pattern with greater noise and scatter, which corresponds to regions near $\cos(\varphi_{diff}) = 0$ boundaries found in Figure 2.9(c); the noise and scatter are expected since Equation (2.25) is indeterminate for $\cos(\varphi_{diff}) = 0$ and since the experimental data would be dominated by the division of small numbers from $\cos(\varphi_{diff})$ in the numerator and denominator. The theoretical wrapped φ_{sum} field in Figure 2.9(b) does not have these poor contrast regions because the theoretical data has exact cancellation of the $\cos(\varphi_{diff})$ in the arctan() formula.

Ghiglia and Romero (1994) developed robust 2D phase unwrapping methods for interferometric fringes with noise. The general phase unwrapping problem is equivalent to the solution to the Poisson's equation with Neumann boundary conditions, which may be solved by fast cosine transform (FCT) methods. With experimental data that may contain noise and measurement errors, the reliability of the wrapped phase information at each pixel should be considered. Since the FCT method cannot incorporate a weight function, a weighted phase unwrapping method based on preconditioned conjugate gradient (PCG) numerical methods was developed. The PCG unwrapping method falls under the category of global minimization, meaning the method attempts to minimize discontinuities globally based on the assumption of a continuous function. If a discontinuity or isolated region is physically allowed in the field as in the case of a regional boundary, then those regions may be weighted such that the PCG algorithm is not required to meet the phase continuity constraint across that region. PCG methods have the added benefit of robust convergence.

The weight function used in this study begins with a quality condition where phase jumps in the wrapped phase of size h_d or nearly zero are considered very reliable with weight of close to one,

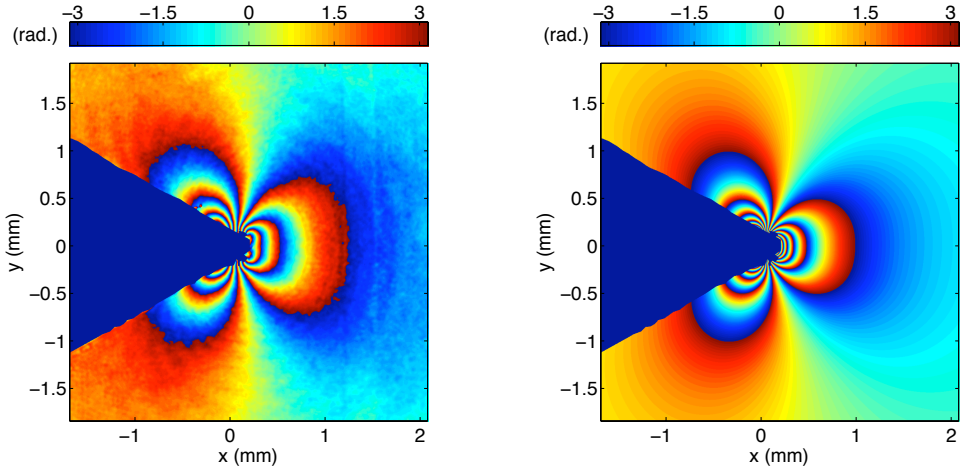

(a) Experimental φ^{Ex}

(b) Theoretical φ^{Ex}

(c) Experimental φ^{Ey}

(d) Theoretical φ^{Ey}

Figure 2.8: Experimental and theoretical wrapped phase maps (in radians) from horizontal shearing CGS with V-notch masked in white: (a) experimental $\varphi^{Ex} = \varphi_{sum} + \varphi_{\alpha d}$; (b) theoretical $\varphi^{Ex} = \varphi_{sum} + \varphi_{\alpha d}$; (c) experimental $\varphi^{Ey} = \varphi_{sum} - \varphi_{\alpha d}$; and (d) theoretical $\varphi^{Ey} = \varphi_{sum} - \varphi_{\alpha d}$

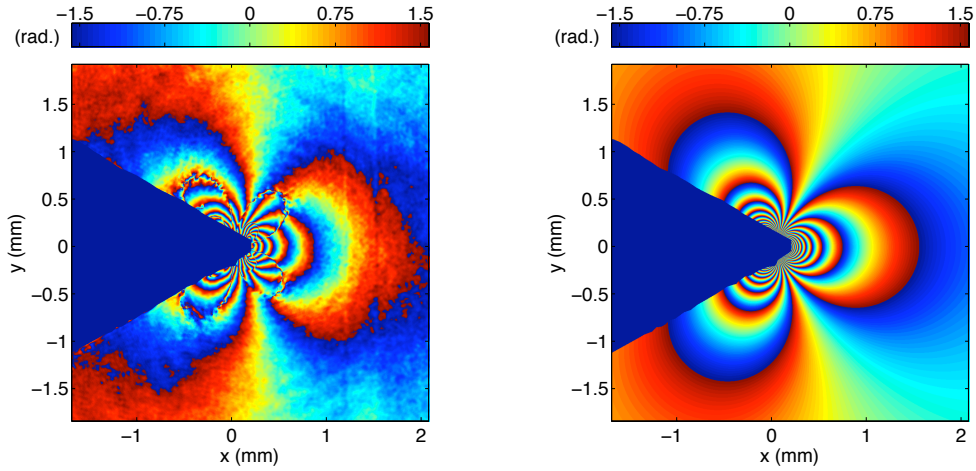

(a) Experimental φ_{sum}

(b) Theoretical φ_{sum}

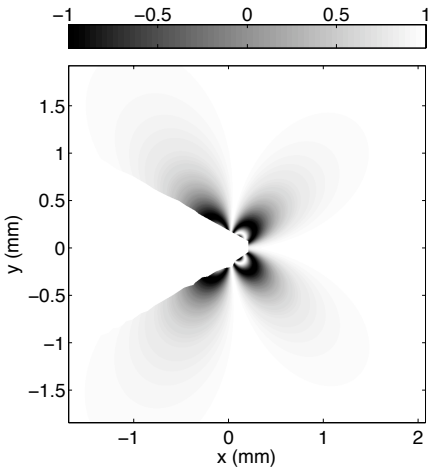

(c) Theoretical $\cos(\varphi_{diff})$

Figure 2.9: Wrapped phase maps from $\lambda/4$ plate method (in radians) with V-notch masked in white: (a) experimental φ_{sum} for $\cos(\varphi_{diff}) \neq 0$; (b) theoretical φ_{sum}; and (c) theoretical $\cos(\varphi_{diff})$ field with its four-lobed clover leaf pattern

while jumps of $h_d/2$ are considered unreliable with weight of zero. The following formula is applied to each pixel to develop the weight function $\mathbf{W}$, where $\Delta\psi_k$ is the wrapped phase difference between the k-th nearest neighbor of the (i, j) pixel (Baldi et al., 2002):

$$W_{i,j} = \prod_{k=1}^{8} \frac{1}{2}\{\cos(2\pi \frac{\Delta\psi_k}{h_d}) + 1\}. \tag{2.28}$$

Additionally, physical boundaries and regions in the field with no photoelastic material, as with the V-notch in the example, are given a weight of zero. Based on *a priori* knowledge of the experiment, the weight of regions with high concentrations of fringes that cannot be resolved with the given pixel resolution are also set to zero to reduce unwrapping errors near these regions.

Figure 2.10 shows the unwrapped φ^{Ex} and φ^{Ey} fields for experimental and theoretical data. The PCG method successfully unwraps the phase discontinuities in these fields; the data from the air in the V-notch region does not propagate into the polycarbonate data due to the weight function; the unwrapped φ^{Ex} and φ^{Ey}, like the theoretical fields, have the general monotonic increase or decrease as $r \to 0$ towards the notch tip.

Figure 2.11(a) is the experimental φ_{sum} determined by the $(\varphi^{Ex} + \varphi^{Ey})/2$, and Figure 2.11(b) is the unwrapped experimental φ_{sum} from the $\lambda/4$ plate method. In comparison, qualitatively, the φ_{sum} field from the $\lambda/4$ plate method does not agree with the theoretical field in Figure 2.11(c) as well as the φ_{sum} from the pure $E_x\hat{\imath}$ and pure $E_y\hat{\jmath}$ fields agrees with the theoretical field; some minor unwrapping errors are evident in Figure 2.11(b) near the $\cos(\varphi_{diff}) = 0$ regions in the four-lobed clover leaf pattern seen in Figure 2.9(c). Additionally, the experimental $\varphi_{\alpha d}$ in Figure 2.11(d) from the $(\varphi^{Ex} - \varphi^{Ey})/2$ has a four-lobed clover leaf pattern like the theoretical $\varphi_{\alpha d}$ field in Figure 2.11(e).

One measure of the global error is the root mean square deviation (RMSD) normalized by the range of experimental data, denoted NRMSD. Only data points not masked by notch mask are considered here. Table 2.2 reports the error analysis of several fields. The NRMSD is low for each of the fields, with the largest error in the φ^{Ey} at only 2.1%. As is evident in Figure 2.12(a) and (b), which show the difference between the theoretical and the two experimental φ_{sum} fields,

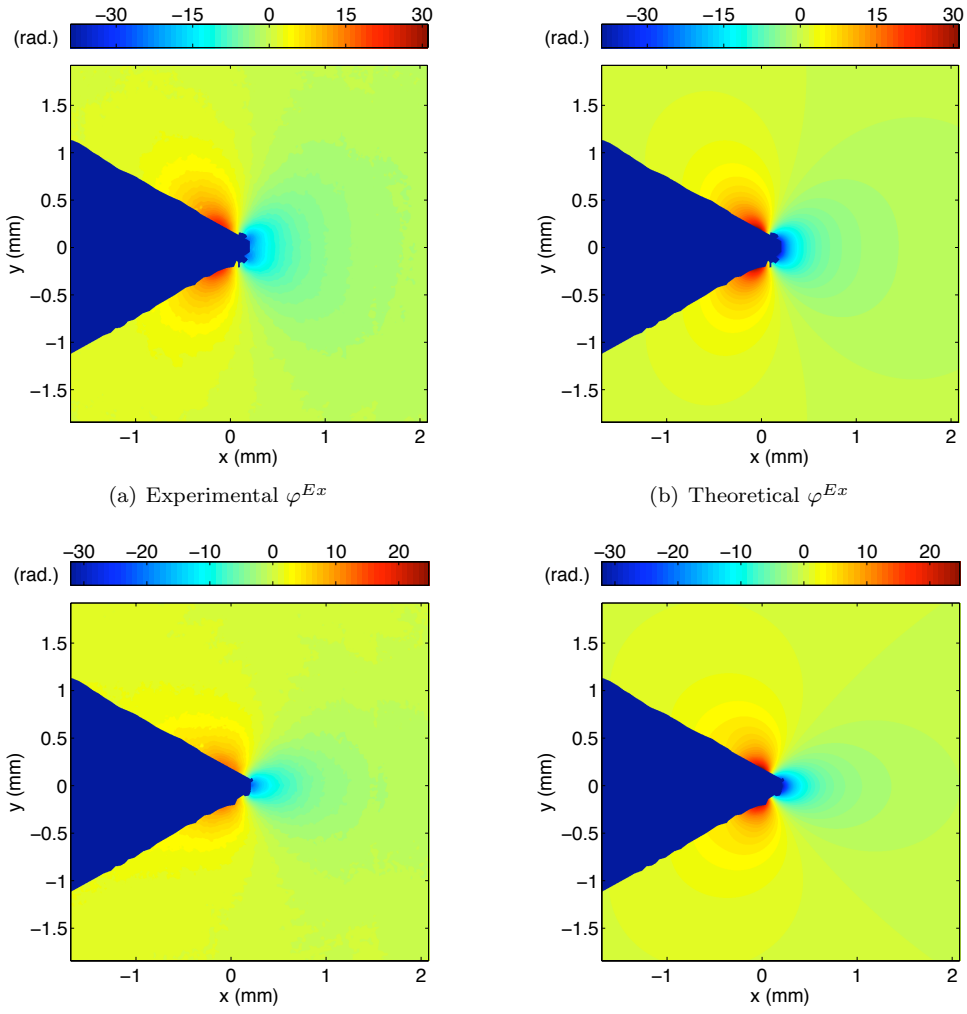

(a) Experimental φ^{Ex}

(b) Theoretical φ^{Ex}

(c) Experimental φ^{Ey}

(d) Theoretical φ^{Ey}

Figure 2.10: Experimental and theoretical unwrapped phase term from the pure $E_x\hat{\imath}$ and pure $E_y\hat{\jmath}$ fields (in radians) from horizontal shearing CGS with V-notch masked in white

the greatest errors are close to the notch tip, which is understandable since the stress derivative changes so rapidly near the notch tip that the small d_{shear} assumption, which allows the phase to be related to stress derivatives in Equation (2.15), breaks down. The unwrapping errors due to the $\cos(\varphi_{sum}) = 0$ regions are in the four-lobed clover leaf pattern in Figure 2.12(b), leading to a slightly higher NRMSD for the φ_{sum} from the $\lambda/4$ plate method than for the φ_{sum} from the pure $E_x\hat{\imath}$ and pure $E_y\hat{\jmath}$ fields data. Both methods of determining φ_{sum} give reasonable global error, though the pure $E_x\hat{\imath}$ and pure $E_y\hat{\jmath}$ fields method does seem to better confine the error to near the notch tip and is not affected by the $\cos(\varphi_{diff})$ issue. Another benefit of the the pure $E_x\hat{\imath}$ and pure $E_y\hat{\jmath}$ fields method

is the determination of $\varphi_{\alpha d}$, which has low error as well; the difference between the theoretical and experimental $\varphi_{\alpha d}$ is shown in Figure 2.12(c), confining the error to near the notch tip. The excellent agreement of the experimental data with theoretical data in this example demonstrates that the use of polarization optics and phase shifting can successfully extract phase data from complicated interference images that have physical meaning in terms of stress in the photoelastic material, as explained in the previous analysis in Section 2.2.2.

Phase	RMSD (in rad.)	Data Range (in rad.)	NRMSD (No units)
φ^{Ex}	0.73	49.14	0.015
φ^{Ey}	0.52	34.05	0.015
φ_{sum} from $\lambda/4$ method	0.72	34.57	0.021
$\varphi_{sum} = (\varphi^{Ex} + \varphi^{Ey})/2$ method	0.57	38.94	0.015
$\varphi_{\alpha d} = (\varphi^{Ex} - \varphi^{Ey})/2$ method	0.26	17.85	0.015

Table 2.2: Error analysis for various experimental fields for horizontal shear

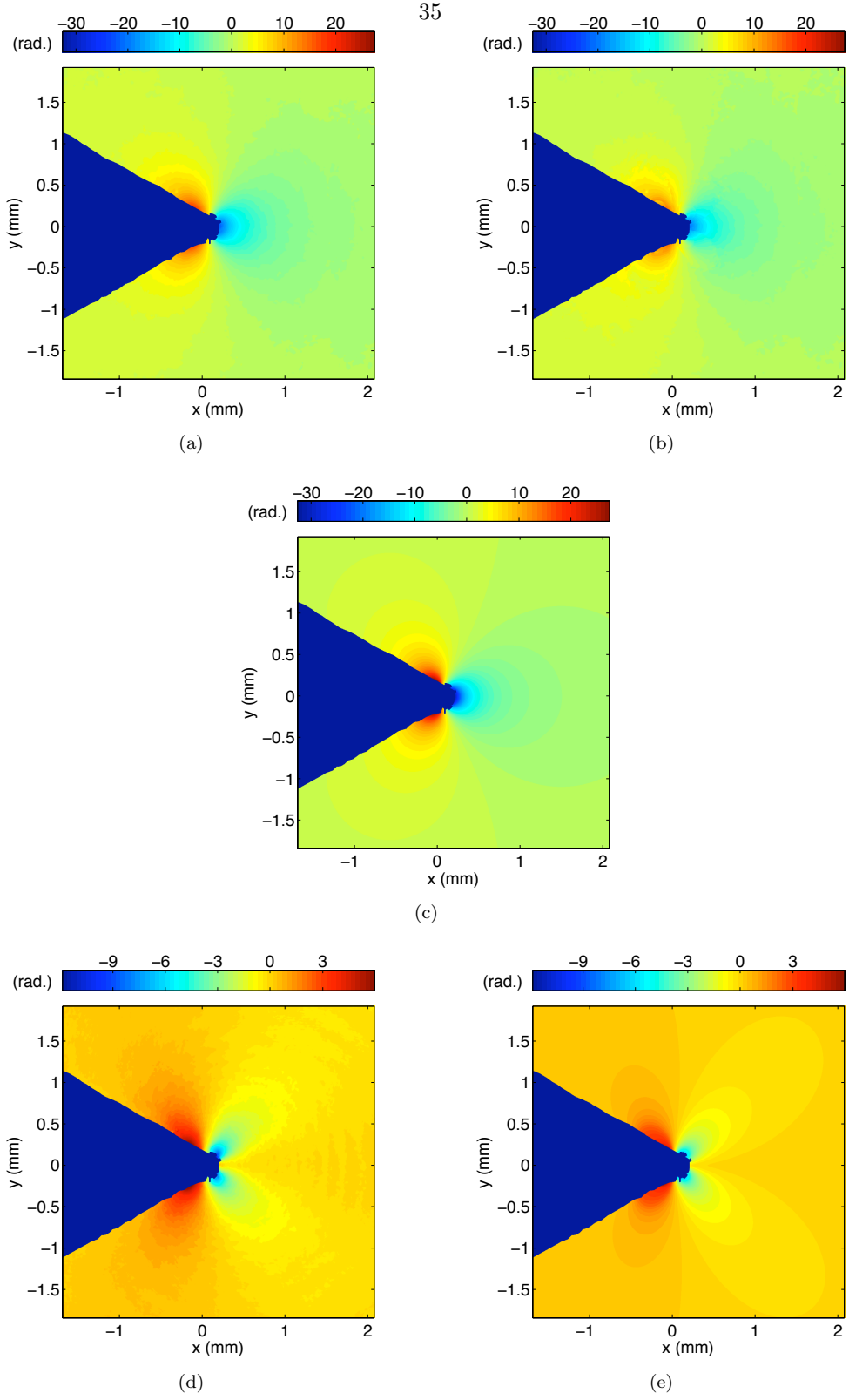

Figure 2.11: Experimental and theoretical phase maps of φ_{sum} and φ_{diff} (in radians) from horizontal shearing CGS with V-notch masked in white: (a) experimental $\varphi_{sum} = (\varphi^{Ex} + \varphi^{Ey})/2$; (b) experimental φ_{sum} from the $\lambda/4$ method (c) theoretical φ_{sum}; (d) experimental $\varphi_{\alpha d} = (\varphi^{Ex} - \varphi^{Ey})/2$; and (e) theoretical $\varphi_{\alpha d}$

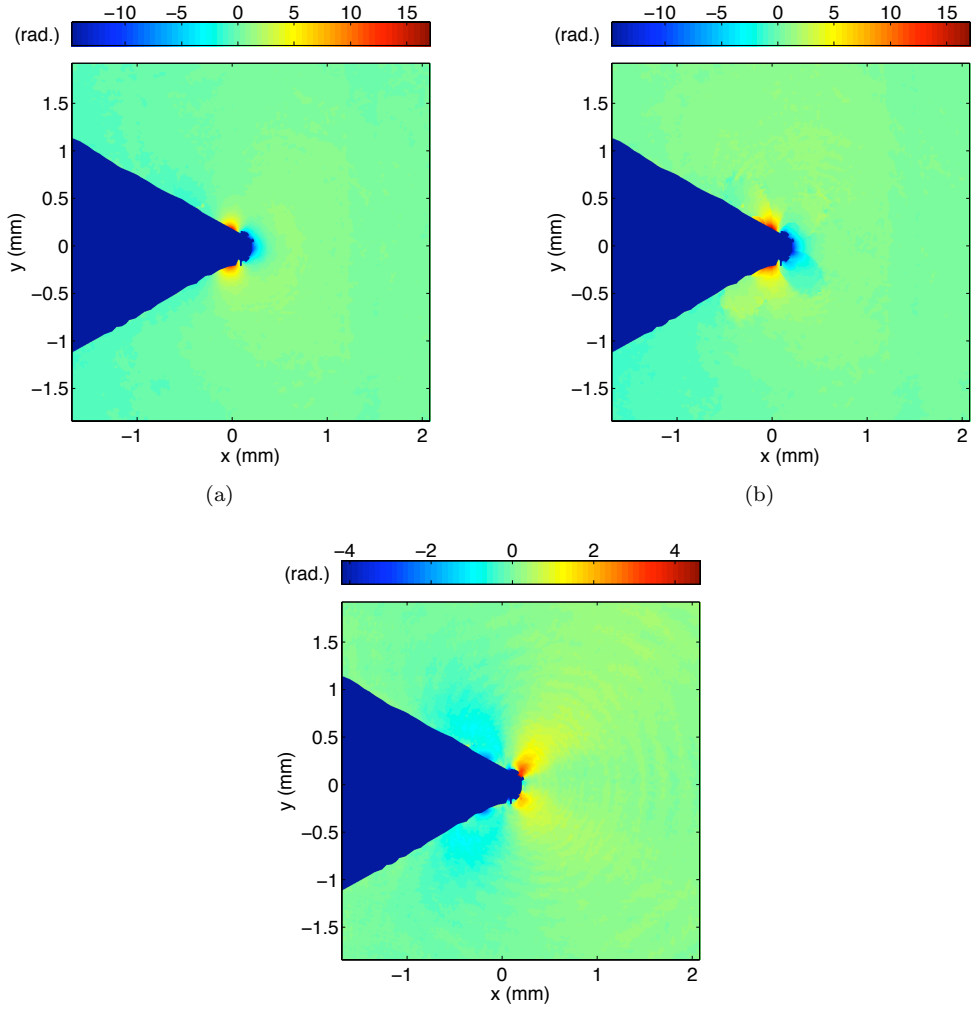

Figure 2.12: Difference between theoretical and experimental φ_{sum} and $\varphi_{\alpha d}$ (in radians) from horizontal shearing CGS with V-notch masked in white: (a) comparison for $\varphi_{sum} = (\varphi^{Ex} + \varphi^{Ey})/2$; (b) comparison for φ_{sum} from the $\lambda/4$ method; and (c) comparison for $\varphi_{\alpha d} = (\varphi^{Ex} - \varphi^{Ey})/2$

2.4 Conclusions

Wavefront shearing interferometry, specifically coherent gradient sensing (CGS), is used to analyze a wavefront transmitted through a photoelastic material. A detailed analysis of the transmitted wavefront properties, of the lateral shearing, and of the resulting interference patterns depending on the polarization of the electric field input to the photoelastic material is provided for a general wavefront shearing interferometer, with some specialization for CGS. Phase information related to stress gradients in a deformed photoelastic material may be extracted from the complicated interference pattern by the use of polarization optics and phase shifting. This is experimentally verified using CGS on a compressed polycarbonate plate with a V-notch. Using this general analysis, stress information may be obtained in full field for photoelastic materials with input electric field polarization control and any phase-shifting transmission wavefront shearing interferometry.